AD-A064 851 DREXEL UNIV PHILADELPHIA PA DEPT OF MATERIALS ENGINEERING F/G 11/4
FATIGUE CRACK PROPAGATION IN A (CO,CR)-(CR,CO)7C3 COMPOSITE.(U)
DEC 78 M H LATIF, A LAWLEY
N00014-76-C-0205

UNCLASSIFIED

NL

1 OF 1
AD
A 064 851

END
DATE
FILMED
4-79
DDC

(12) LEVEL II

AD A064851

DDC FILE COPY

Drexel University

DISTRIBUTION STATEMENT A
Approved for public release;
Distribution Unlimited

DDC
RECEIVED
FEB 23 1979
B

79 02 16 096

(12) LEVEL II

AD A064851

DDC FILE COPY

(6)

FATIGUE CRACK PROPAGATION IN A $(Co,Cr)-(Cr,Co)_7C_3$ COMPOSITE

(10) M. H. Abdel/Latif and A./Lawley

(11) December 1978

(9) Technical Report

(12) 34 p.

Office of Naval Research
Arlington, Virginia 22217

(15) Contract #N00014-76-C-0205

Distribution of this document is unlimited

Drexel University
Department of Materials Engineering
Philadelphia, Pa. 19104

409592

79 02 16 095

ABSTRACT

Fatigue crack propagation in the Co, Cr-$(Cr,Co)_7C_3$ in-situ composite has been characterized at room temperature in the as-grown condition and following past solidification isothermal exposure or thermal cycling. The dependence of da/dN on ΔK follows the Paris-Erdogan relation over the range $\Delta K \sim 10$ MN.m$^{-3/2}$ to $\sim$50 MN.m$^{-3/2}$. Fracture toughness is low in the as-grown condition and is attributed to restricted matrix slip and a low stacking fault energy in the cobalt-rich matrix coupled with the absence of delamination. The heat treatments enhance fracture toughness and this is shown to be the result of precipitation of $(Co,Cr)_{23}C_6$ in the matrix and/or fiber coarsening with an attendant increase in the interfiber spacing. At the lower end of the ΔK range fatigue cracking is primarily crystallographic (stage I) in nature. Stage II cracking, with the fracture surface normal to the stress axis, is operative at the upper end of the ΔK range; the transition occurs between 17 MN.m$^{-3/2}$ and 28 MN.m$^{-3/2}$. The fracture toughness of Co,Cr-$(Cr,Co)_7C_3$ is inferior to CoTaC or the lamellar γ/γ'-δ and γ-δ in-situ composites. These differences are rationalized in terms of constituent matrix and fiber properties.

Introduction

Fatigue crack propagation (FCP) behavior has recently been examined in a number of nickel-base (1-6) and cobalt-base (1,3) superalloys. These studies have provided a partial understanding of the role and interdependence of microstructure, stress intensity level, load cycle frequency, and temperature on resistance to crack propagation. The potential of directionally solidified (in-situ) high-temperature eutectic composites as an alternative to the superalloys in gas turbine components has resulted in the application of fracture mechanics concepts to this class of new materials. While the data base is still limited, FCP rates have been reported for lamellar Ni-Ni_3Nb (γ-δ) (7), Ni/Ni_3Al-Ni_3Nb (γ/γ'-δ) (8), and rod-like Cotac (9) and (Co,Cr), - Cr_7C_3(8,10).

In the present study, the FCP response of (Co,Cr)-$(Cr,Co)_7C_3$ has been determined at room temperature in terms of the dependence of the rate of crack propagation (da/dN) on stress intensity range (ΔK). Particular attention was directed to the effect(s) of post-solidification heat treatments simulating gas turbine service environments; these included several regimes of elevated-temperature isothermal exposure and thermal cycling. The only other data on FCP at room temperature in this composite is that reported by Scarlin (10). Yuen and Leverant (8) measured FCP rates in (Co,Cr)-$(Cr,Co)_7C_3$ at 760°C and 927°C. No influence of fiber spacing on FCP rates was noted; this was attributed to the large plastic zone size at the crack tip, relative to the interfiber spacing. It was also observed that failure of the carbide fibers ahead of the crack tip did not occur, even though the calculated plastic zone size was greater than the interfiber spacing. Scarlin (10) also examined FCP as a function of temperature and rationalized comparative propagation rates in terms of the properties of the matrix, which shows a phase transformation at ~850°C. Neither Yuen and Leverant (8) or Scarlin (10) included post-solidification thermal treatments in their studies on FCP in Co,Cr-$(Cr,Co)_7C_3$.

Experimental Procedure

A. Composite Preparation

Master alloy rods were prepared from 99.99% purity cobalt and chromium and spectrographic grade carbon by induction melting in an alumina crucible under argon and casting in a stainless steel mold. The overall composition of the alloy was Co-41%Cr-2.4% C by weight. Ingots 14.29 mm diameter x 177.8 mm in length were then prepared by directional solidification of the master alloy rods in closed alumina tubes under a dynamic argon atmosphere. The induction furnace was similar to that used by Thompson et al. (11) and has been described by Saatchi (12). The growth rate (R) was 7×10^{-6} m/s with a temperature gradient (G) $\sim 25 \times 10^{3}$°C/m at the liquid-solid interface of the composite. One ingot was directionally solidified at a higher growth rate (R) of 47.6×10^{-6} m/s. The corresponding G/R values at the two growth rates (36×10^{8}°C s/m^2 and 5.3×10^{8}°C s/m^2, respectively) resulted in an aligned rod-like reinforcement of $(Cr,Co)_7C_3$ in a cobalt-rich matrix at a volume fracture $V_f = 0.3$.

B. Post-Solidification Treatments

The directionally solidified ingots were subsequently given one of four regimes of thermal treatment: (1) isothermal exposure at 913°C (T/T_m = 0.75) for times up to 15×10^{5}s; (2) isothermal exposure at 1121°C (T/T_m = 0.87) for times up to 26×10^{5}s; (3) thermal cycling between 79°C and 913°C up to 465 cycles; (4) thermal cycling between 79°C and 1121°C up to 700 cycles. The times per cycle (T_{min} to T_{max} to T_{min}) were 1250 s (60 s heating/1190 s cooling) and 1700 s (200 s heating/1500 s cooling) for thermal cycling regimes (3) and (4) respectively.

For isothermal annealing, the ingots were sealed in quartz capsules under argon. Specimens for thermal cycling were placed in a quartz tube under flowing argon and located along the focal axis of a radiant heat reflector furnace. The latter consisted of two quartz lamps with a heating zone 254 mm

in length. A temperature controller and recorder were coupled to the furnace so that T_{min} and T_{max} could be preset to ±2°C.

C. Fatigue Testing

The relatively small size of the directionally solidified ingots precluded the use of a conventional fatigue specimen. In consequence, a four-point bending configuration was selected for the determination of FCP rates. Specimens were 12.7 mm x 2.54 mm x 114.3 mm, Figure 1(a), similar to those used by Mills and Hertzberg (7) for fatigue studies on γ-δ. Specimens were ground to size with the direction of fiber reinforcement parallel to the long dimension of the test piece. A starting notch (1.27 mm deep x 0.152 mm wide) was introduced normal to the long dimension at the center of the specimen by EDM; thus, the overall direction of crack propagation was perpendicular to the reinforcing carbide. The four-point bend apparatus had a major span of 101.6 mm and a minor span of 76.2 mm, Figure 1(a).

Cyclic tests were performed at room temperature on an MTS electro-hydraulic closed loop machine in tension-tension loading with a sinusoidal load-time form at 12.5 Hz. The stress ratio (R_c = min. stress/max. stress) was equal to 0.1 or 0.5.

Initially, attempts were made to determine incremental crack extension by periodically interrupting the test in order to measure crack extension by means of a travelling microscope. This approach was unsuccessful since crack propagation rates were relatively high and the crack advanced across virtually the entire width (W) of the specimen before a sufficient number of readings could be taken. To determine FCP rates, it was necessary to use a crack opening displacement gage in order to continually monitor progress of the crack. The gage was attached to the specimen across the notch by means

of two knife edges and the gauge output corresponding to a specific applied load and crack length recorded. This was repeated for different known crack lengths in order to establish the relationship between specimen compliance and crack length. During cycling, the output of the gage was monitored continuously; this was helpful in selecting the load and cycle intervals over which crack extension measurements were made. Details of the calculation of ΔK and da/dN are given in Appendix I. A photograph of the complete bend facility with a specimen in place is shown in Figure 1(b).

D. Metallography

Microstructures were examined in the as-grown condition, after each of the four heat treatments, and following fatigue testing. Several cyclic tests were interrupted to characterize microstructural damage ahead of the crack tip.

Specimens were wet ground through 600 grit paper, rough polished with diamond paste and given a final polish using Linde A and B aluminum oxide powder. For optical metallography, the polished surface was lightly etched in aqua regia. Specimens were also deep etched in boiling aqua regia to partially remove the matrix; in this condition, the composite was examined by scanning electron microscopy to reveal carbide morphology. Fatigue fracture surfaces were also examined in the scanning electron microscope.

Experimental Results and Observations

A. Microstructures

Representative optical micrographs of the composite in the as-grown condition are illustrated in Figure 2; transverse and longitudinal sections are included for both growth rates employed. Scanning electron microscopy provides a three-dimensional characterization of the carbide-fiber morphology, Figures 2(e) and 2(f). Consistent with previous observations on this composite (13), the aligned fibrous carbide reinforcement is highly irregular in terms

of cross-sectional dimensions and geometry. Carbide branching is evident and the aspect ratio varies over a wide range. Interfiber spacing and fiber diameter were measured and found to vary about a mean of 3.53μm and 2.03μm respectively for the growth rate of 7×10^{-3} mm·s^{-1}. Corresponding values were 1.5μm and 0.86μm for growth at 47.6×10^{-3} mm·s^{-1}. Faceting of fiber cross-sections is evident in Figures 2(a), 2(c), 2(e) and 2(f). This reflects the hexagonal symmetry of the carbide fibers.

The effect of thermal cycling and isothermal exposure on the microstructural stability of Co,Cr-$(Cr,Co)_7C_3$ has been examined in detail by Saatchi (12) and Lawley et al. (14-16). These studies included the four regimes selected in the present study and the observations may be summarized as follows:

1. Isothermal annealing at 913°C results in a degeneration of the carbide fibers in that small branches develop on the fibers. These grow out from the main fibers into the matrix and subsequently break up to produce discrete precipitates approximately spherical in shape, Figure 3. Branching has been observed at times ≥ 25.9×10^4s and the number of branches increases with time. Energy dispersive analysis (12) confirms that the precipitates are $(Cr,Co)_{23}C_6$, consistent with previous work by Thompson et al. (13) on this composite system and observations by Lane and Grant (17) on the stability of Cr_7C_3. Thus, at 913°C the composite consists of $(Cr,Co)_{23}C_6$ precipitates and $(Cr,Co)_7C_3$ fibers in a cobalt rich matrix.

2. There is no evidence of the $(Cr,Co)_7C_3$ precipitate following isothermal annealing at 1121°C for times up to 25.9×10^5s, Figure 4. However, microstructural instability is reflected in two-dimensional coarsening (Ostwald ripening) of the $(Cr,Co)_7C_3$ carbide reinforcement with an associated decrease in rod density (# of rods per unit area). The

effect is more pronounced in composites grown at the higher rate (47.6×10^{-3} mm/s) since fiber diameter and interfiber spacing in the as-grown condition are smaller than for the lower growth rate (7×10^{-3} mm/s). In the absence of precipitation of $(Cr,Co)_7C_3$, the fiber surfaces remain smooth.

3. No fiber branching or precipitation in the matrix occurs after cycling between 79°C and 913°C, at least up to 465 cycles, Figure 5. Over the temperature range 79°C to 1121°C, some fiber branching is seen after 700 cycles, Figure 6.

B. Crack Propagation Response

Because of the high strength and relatively low fracture toughness of the composite at room temperature, the plastic zone size is small in relation to overall crack length. In the discussion, it is calculated that the plastic zone size: crack length ratio is ≤ 0.03 and any effect of plastic flow at the advancing crack tip on FCP has been ignored in this study.

The fatigue crack propagation behavior of the composite in the directionally solidified condition is shown in Figure 7; two stress ratios are included, namely 0.1 and 0.5. Data are also given for the cast (non-controlled growth) eutectic composite. Crack propagation curves as a function of ΔK for the composite following isothermal exposure at 913°C and 1121°C are presented in Figures 8 and 9 respectively. The corresponding dependence after the two thermal cycling regimes is shown in Figures 10 and 11.

In each of the above conditions, the FCP response approximates the Paris-Erdogan relationship (18):

$$da/dN = A(\Delta K)^m \qquad (1)$$

where A and m are constants; m is a measure of the fracture toughness of the material. Values of the exponent m are given in Table I for the composite in

each of the conditions examined. Also included are values of the minimum (threshold) levels of ΔK (i.e. ΔK_{TH}) necessary for crack propagation, and the critical stress intensity range ΔK_C at which the crack becomes unstable. For purposes of comparison, FCP parameters reported by other workers for this and other in-situ composites are listed in Table I.

At a stress ratio R = 0.1, the directionally solidified and cast materials exhibit similar FCP response in terms of m (Figure 7 and Table I). However, for a given level of ΔK, crack propagation rate is lower in the aligned composite than in the non-controlled (cast) eutectic. These high values of m reflect poor fracture toughness at ambient temperatures. Increasing the stress ratio from 0.1 to 0.5 results in a significant decrease in m from 29 to 10, Figure 7 and Table I. However, the level of ΔK required to give a specific crack propagation rate da/dN is lower at R = 0.5 than at R = 0.1.

All fatigue testing on the in-situ composite following post-solidification heat treatment was carried out at a stress ratio R = 0.1. Both isothermal exposure and thermal cycling result in an increase in fracture toughness compared to the as-grown condition, as reflected in lower m values, Table I. For comparison, the da/dN versus ΔK curve for the as-grown (DS) composite (R = 0.1; growth rate 7×10^{-6} m/s) is included in each of Figures 8-11. Figure 12 affords an overall comparison of FCP behavior as a function of post-solidification heat-treatment.

From Figure 8 it is seen that isothermal exposure at 913°C results in inferior crack propagation resistance (da/dN) to the DS condition at $\Delta K \leq 30$ MN.m$^{-3/2}$. Above this stress intensity range, the reverse holds true.

Long-time isothermal exposure (25.9×10^5s) at 1121°C results in a significant improvement in both fracture toughness (lower m) and resistance to crack propagation (da/dN) at a given ΔK, relative to the DS condition, Figure 9. This figure also shows that for a fixed exposure time of 4.32×10^5s, the composite directionally solidified at the higher growth rate exhibits the better resistance to crack propagation over the ΔK range studied. However, the slope m is higher for the composite grown at the higher rate.

After thermal cycling between 79°C and 913°C, the plots of da/dN versus ΔK lie below the plot for the DS composite, Figure 10. This enhanced resistance to crack propagation is coupled with enhanced fracture toughness, i.e., m = 18. Thermal cycling between 79°C and 1121°C leads to an increase in fracture toughness (lower m) over the DS condition. Resistance to crack propagation after thermal cycling over this temperature range is superior to that in the DS condition at ΔK levels $\geq$ 28 MN.m$^{-3/2}$, Figure 11.

The location of the various FCP plots for the heat-treated composites, relative to that of the DS material, is illustrated in Figure 12. With the exception of line D, each lies close to line A for the DS material, but with a lower slope. Long-time exposure at 1121°C results in increased fracture toughness and resistance to crack propagation, as reflected in the slope of line D and its displacement to higher ΔK levels, relative to line A.

C. Fracture Morphology

Optical micrographs of sections approximately perpendicular to the fracture surfaces of the non-aligned (cast) and directionally solidified (as-grown) composite are compared in Figure 13. In the non-aligned casting, there is no evidence of cracking of carbide particles; matrix cracks follow the contour of the carbides, Figure 13(a). There was no evidence

for carbide cracking below the main fracture surface in the aligned composite, Figures 13(b) and 13(c). However, secondary cracks are present in the matrix but are blocked by the carbide fibers, Figures 13(b) and 13(c).

Similarly, no fiber cracking is observed ahead of the advancing crack tip, Figure 14(a). The main crack path is compared at low ΔK ($\sim$22 MN.m$^{-3/2}$) and high ΔK ($\sim$31 MN.m$^{-3/2}$) levels in Figures 14(b) and 14(c) respectively. At a low ΔK, the main crack propagates either through fibers or around fiber ends; infrequently, the crack is observed to run parallel to the long dimension of the fiber, Figure 14(b). At high ΔK levels, cracks always propagate directly through the carbide fiber reinforcement. Under this condition, crack branching has been observed, Figure 14(c).

Scanning electron micrographs of the fracture surfaces at low and high ΔK levels are compared in Figures 15(a) and 15(b). In the former, cracking occurs primarily along active slip planes of the matrix (stage I). At high ΔK levels, the overall direction of the fracture surface is normal to the applied stress axis (stage II). No fatigue striations were observed. A transition from the stage I to the stage II propagation mode is suggested for ΔK between 17 MN.m$^{-3/2}$ and 28 MN.m$^{-3/2}$.

Discussion

A. FCP - As Grown Condition

The FCP response of Co,Cr-(Cr,Co)$_7$C$_3$ and other in-situ composites at room temperature is compared in Figure 16. Also included is the curve for Haynes Alloy 188 which is a cobalt-base solid solution strengthened superalloy (19). A discrepancy exists between the room temperature FCP response of Co,Cr-(Cr,Co)$_7$C$_3$ determined in the present study and that reported by Scarlin (10). The difference in location and slope of the two curves for Co,Cr-(Cr,Co)$_7$C$_3$ at room temperature is seen more clearly in Figure 17. In both studies the material composition and stress ratio were identical, and growth rates were similar. Scarlin used

non-conventional single edge notched specimens with deep face grooves. While Scarlin did not report fracture morphologies at room temperature, at 750°C cracks run in parallel pairs perpendicular to the fiber direction. As noted by Scarlin, interaction between the two cracks will cause a reduction in the local level of ΔK; this would displace Scarlin's curve to the left (lower ΔK) and may in part be responsible for the difference. It should also be noted that Scarlin's data only fit the Paris-Erdogan relation over a narrow ΔK range, Figure 17. At the high end of the ΔK range, the slope of Scarlin's curve for room temperature FCP is comparable to that determined in this study ($m \sim 29$).

From Figure 16 and a comparison of m values (Table I), it is clear that at ambient, the aligned Co,Cr-$(Cr,Co)_7C_3$ composite displays inferior fracture toughness in cyclic loading to the rod-like CoTaC and the lamellar γ/γ'-δ and γ-δ structures. Likely contributing factors include (1) a low matrix stacking fault energy, (2) a restricted number of matrix slip systems, (3) strong matrix-fiber interface bonds. Each is now considered.

- The cobalt-rich matrix is expected to have a low stacking fault energy. In consequence dislocations are confined to their slip planes, giving rise to planar slip and to stress concentrations which lead to matrix cracking along these planes. These conditions are conducive to fiber shearing, as observed in this study, with a corresponding low resistance to FCP. For a given ΔK level, the Haynes alloy (19) exhibits superior fracture toughness and resistance to FCP (i.e. lower da/dN), Figure 16. While the matrix compositions of the Haynes alloy and that of the composite are different, the deformation behavior should be similar. Hence the lower FCP resistance and fracture toughness of the composite is vested in the presence of the carbide fibers and the associated higher strength level of the composite (1875 MPa) compared to the solid-solution strengthened superalloy (1027 MPa).

- At room temperature, the cobalt-rich matrix has a hexagonal close-packed structure with a limited number of operative slip systems. This coupled with a low stacking fault energy promotes stress concentration at the crack tip and low fracture toughness. The observed temperature dependence of FCP response (Figure 17) is consistent with this reasoning. At 950°C the matrix is face centered cubic (20) with its inherent multiplicity of available slip systems, so that the capacity of the matrix for deformation is increased along with resistance to FCP (21). Scarlin's curve for FCP at 950°C lies to the right (higher ΔK levels) of the room temperature curves from this and Scarlin's study (10). The low FCP resistance observed by Scarlin (10) at 750°C (Figure 17) reflects retention of the close-packed hexagonal matrix structure (21) coupled with a minimum in both ductility (22) and impact resistance (23) at this temperature.

  Yuen and Leverant's material contained 4% Ni and 2.5% Al by weight (8). According to Scarlin (10) this stabilizes the fcc structure of the matrix down to room temperature. While their FCP curves at 760°C and 927°C reflect good fracture toughness (m = 5.7 and 2.3), Figure 17, it would be expected that they lie close to or to the right of the room temperature curves. Clearly this is not the case.

- The interfacial matrix-carbide bond in the Co,Cr-$(Cr,Co)_7C_3$ composite is strong. This is confirmed by a lack of fiber pull-out or interface delamination in this study and under static or impact loading (12, 15, 16). In contrast, cycle loading gives rise to crack deflection and delamination in lamellar γ/γ'-δ (8), and interface delamination and deformation twinning of the δ phase in lamellar γ-δ with

subsequent twin boundary fracture (24). Crack deflection lowers the effective ΔK and improves fracture toughness since the crack has to be reinitiated. Each provides an effective crack resisting mechanism which is absent in the cobalt matrix composite.

Neither Yuen and Leverant (8) nor Scarlin (10) reported fracture morphologies at room temperature. At 927°C carbide fibers did not break ahead of the main fatigue crack (8), consistent with the present observations. Similarly Scarlin (10) reports flat fractures at 720°C with crack propagation primarily through the carbide fibers.

It is interesting to note that Yuen and Leverant (8) were unable to measure FCP rates at room temperature in (Co,Cr)-$(Cr,Co)_7C_3$. They reported a tendency for the crack to grow crystallographically (stage I), possibly by faceted cleavage cracking along active slip planes in the matrix. At 760°C and 927°C stage II cracking predominated. SEM observations of fracture surfaces by Austin et al. (9) on CoTaC and Jablonski et al. (19) on Haynes alloy following FCP at room temperature showed the same dependence of fracture mode on ΔK as that observed in the present study. Specifically, at low ΔK the transgranular crack path was strongly crystallographic (stage I). With increasing ΔK, the appearance of the fracture surface changed such that increasing proportions of cracking normal to the applied stress axis developed (stage II). While striations were evident on the stage II fracture surface of the superalloy, no striations were observed in the CoTaC composite; in our study no striations were found on fracture surfaces of the Co,Cr-$(Cr,Co)_7C_3$ composite.

B. FCP - Effect of Heat Treatment

As outlined previously, the major microstructural changes occurring during post-solidification heat-treatment involve the formation of a fine-scale precipitate of $(Cr,Co)_{23}C_6$ and/or coarsening of the rod-like carbide reinforcement. The latter is most advanced after 25.9×10^5s at 1121°C and this treatment does not give rise to a breakdown of the $(Cr,Co)_7C_3$ to the $M_{23}C_6$ form. It can therefore be concluded that the significant enhancement in both fracture toughness and resistance to FCP relative to the DS condition (cf curves A and D in Figure 12) is due to the increase in interfiber spacing (λ) and fiber diameter.

Quantitatively, it has been shown that the above isothermal exposure increases λ from 3.53μm to 7.4μm with a corresponding decrease ∿77% in rod density (16). Similarly, this long-time exposure at 1121°C resulted in a two-fold increase in the work of fracture at room temperature over that in the DS condition (16). This is entirely consistent with the expected dependence of impact response on fiber diameter. The model of Cooper and Kelly (25) predicts the observed increase in the work of fracture with increasing fiber diameter. Similarly, increases in impact resistance have been reported by Thompson (26) in this composite and by Yue and Kaba (27) in unidirectionally solidified $Ti-Ti_5Ge_3$.

It is postulated that the precipitates of $(Cr,Co)_{23}C_6$ act to locally deflect the advancing fatigue crack and so effectively reduce da/dN and the sensitivity to ΔK. Their role is analogous to that of delamination at matrix-fiber interfaces in $\gamma/\gamma'-\delta$ or $\gamma-\delta$. The recent observations by Scarlin (10) on creep crack propagation support this explanation. Thus, the $(Cr,Co)_{23}C_6$ precipitate develops in bands (rings) around the remaining $(Cr,Co)_7C_3$ fibers and the creep crack is deflected at, and propagates for short distances along, the

bands (i.e., parallel to the direction of reinforcement) before continuing in a direction perpendicular to the applied stress.

Of the four post solidification heat-treatments, curves B and F in Figure 12 reflect the presence of the $M_{23}C_6$ carbide precipitate; curves C and E do not though some coarsening will have occurred in each. An explanation for the increase in fracture toughness evidenced by the curves C and E, relative to curve A is currently lacking.

C. Effect of Carbide Spacing

In contrast to the FCP results of the present study, Yuen and Leverant (8) did not observe any effect of solidification rate on crack response in Co,Cr-$(Cr,Co)_7C_3$. This indpendence was explained by the large plastic zone size at the crack tip relative to the interfiber spacing. The cyclic plastic zone size at the crack tip (r_y^c) is given by (28):

$$r_y^c = 0.033 \left(\frac{K}{\sigma_y^c}\right)^2 \qquad (2)$$

where σ_y^c is the cyclic yield stress. Assuming σ_y^c is approximately equal to the monotonic tensile yield stress (517 MN/m^2), and with a minimum value of 11 $MN.m^{-3/2}$ for ΔK, $r_y^c \approx 15\mu m$. This is larger than the interfiber spacings present in the present study (1.5μm and 3.5μm) so that a growth rate effect is not expected. However, the increased FCP resistance associated with the higher growth rate (Figure 9) could be the result of its higher strength level making crack initiation more difficult in this condition. The ultimate compressive strength levels at the low and high growth rates are 1875 MN/m^2 and 2275 MN/m^2, respectively. It must also be noted that the FCP data reported by Yuen and Leverant (8) refer to elevated temperatures (760°C and 927°C).

Because of the high strength and low fracture toughness of the composite at room temperature, the plastic zone size (r_y^c) is small in relation to the

overall crack length. The plastic zone size of 15μm calculated above represents a minimum value. At the highest ΔK levels, the ratio of plastic zone size to crack length is typically ∿0.03. Thus the effect of the plastic zone at the crack tip on FCP has been ignored in the present study.

Conclusions

1. FCP response of the in-situ Co,Cr-$(Cr,Co)_7C_3$ composite at room temperature approximates the Paris Erdogan relation over the range $\Delta K \sim 10$ MN.m$^{-3/2}$ to ~ 50 MN.m$^{-3/2}$.

2. Fracture toughness is low in the directionally solidified condition (m = 29) and is attributed to the low stacking fault energy of the matrix, a restricted number of slip systems and to the absence of crack deflection or interface delamination.

3. Post solidification heat treatments involving elevated temperature (isothermal) exposure or thermal cycling enhance fracture toughness. This is due to the development of a fine-scale precipitate of $(Co,Cr)_{23}C_6$ in the cobalt-rich matrix and/or fiber coarsening with an associated increase in interfiber spacing.

4. At low ΔK levels, the fatigue crack is crystallographic in nature (stage I) but is normal to the applied stress at a higher ΔK. The transition is in the range 17 MN.m$^{-3/2}$ to 28 MN.m$^{-3/2}$.

5. The fracture toughness of Co,Cr-$(Cr,Co)_7C_3$ is lower than that of CoTaC and lamellar γ/γ'-δ or γ-δ.

Acknowledgment

The authors express their gratitude to Mr. R. DeLaVaux at the Laboratory for Research on the Structure of Matter, University of Pennsylvania, for assistance with the fatigue testing. Dr. Abdel Latif is a member of the faculty of the Production Engineering Department, Ain Shams University, Cairo.

References

1. D. F. Mobray, D. A. Woodford and D. E. Brandt, ASTM STP #520, 1973, Am. Soc. for Testing and Mats., p. 416.

2. R. B. Scarlin, Met. Trans. A, 1976, Vol. 7A, p. 1535.

3. D. A. Jablonski, J. V. Carisella and R. M. Pelloux, Met. Trans. A, 1977, Vol. 8A, p. 1893.

4. H. F. Merrick and S. Floreen, Met. Trans. A, 1978, Vol. 9A, p. 231.

5. S. Puroshothaman and J. K. Tien, Met. Trans. A, 1978, Vol. 9A, p. 351.

6. M. Clavel and A. Pineau, Met. Trans. A, 1978, Vol. 9A, p. 471.

7. W. J. Mills and R. W. Hertzberg, ASTM STP #569, 1975, Am. Soc. for Testing and Mats., p. 5.

8. A. Yuen and G. R. Leverant, Met. Trans. A, 1976, Vol. 7A, p. 1443.

9. C. M. Austin, N. S. Stoloff and D. J. Duquette, Met. Trans. A, 1977, Vol. 8A, p. 1621.

10. R. B. Scarlin, Met. Trans. A, 1977, Vol. 8A, p. 1941.

11. E. R. Thompson, F. D. George and E. M. Breinan, Proceedings Conf. on In-Situ Composites, National Materials Advisory Board, National Academy of Sciences, 1973, #308, p. 71.

12. H. Saatchi, "Microstructural Stability and Strength of the Monovariant Co,Cr-$(Cr,Co)_7C_3$ Composite", June 1978 Ph.D. Thesis, Drexel University, Philadelphia, Pa.

13. E. R. Thompson and F. D. Lemkey, Met. Trans. A, 1970, Vol. 1A, p. 2799.

14. Y. Taniyama and A. Lawley, "Elevated Temperature Stability of a Co-Cr-C In-Situ Composite"in Proc. Conf. on In-Situ Composites III; Materials Research Society, in press.

15. L. Y. Lin, M. H. AbdelLatif and A. Lawley, Proceedings 2nd International Conference on Composite Materials, The Metallurgical Society of AIME, Editors, R. Noton, R. Signorelli, K. Street and L. Phillips, p. 770 (1978).

16. M. H. AbdelLatif and A. Lawley, "The Effect of Thermal Treatments on the Structure and Tougness of (Co,Cr)-$(Cr,Co)_7C_3$," submitted to Met. Trans.

17. J. R. Lane and N. J. Grant, Trans. ASM, 1952, Vol. 44, p. 113.

18. P. C. Paris and F. Erdogan, J. Basic Eng., Trans. ASME, 1963, Series D, Vol. 85, p. 528.

19. D. A. Jablonski, J. V. Carisella and R. M. Pelloux, Met. Trans. A, 1977, Vol. 8A, p. 1893.

20. E. R. Thompson, D. A. Koss and J. C. Chesnutt, Met. Trans. A, 1970, Vol.1A, p. 2807.

21. M. Gell and G. R. Leverant, ASTM, STP, 1973, #520, p. 37.

22. R. B. Scarlin, Mats. Sci. and Eng., 1975, Vol. 21, p. 139.

23. P. R. Sahm and T. Varga, see reference #11, Vol. II, p. 239.

24. W. R. Hoover and R. W. Hertzberg, Met. Trans. A., 1971, Vol. 2A, p. 1289.

25. G. A. Cooper and A. Kelly, J. Mech. Phys. Solids, 1967, 15, #4, p. 279.

26. E. R. Thompson, J. Composite Mats., 1971, Vol. 5, p. 235.

27. A. S. Yue and B. T. Kaba, ASTM STP, 1975, #580, p. 504.

28. J. R. Rice, ASTM STP, 1966, #415, p. 247.

29. W. F. Brown and J. E. Strawley, ASTM STP, 1966, #410.

Table I. FCP Parameters of Co,Cr-$(Cr,Co)_7C_3$ and Other In-Situ Composites

Composite	Condition	m	ΔK_{TH}^{*} ($MNm^{-3/2}$)	ΔK_{C}^{**} ($MNm^{-3/2}$)	Reference
Co,Cr-$(Cr,Co)_7C_3$	DS†; R = 0.1†† G.R.††† 7 x 10^{-6}m/s R.T.††††	29	21	32	This study
"	DS; R = 0.5 G.R. 7 x 10^{-6}m/s; R.T.	10	8	25	"
"	Non-aligned (as-cast), R.T.	23	16	27.5	"
"	DS+10.37x10^5s at 913°C	15	14	31.3	"
	DS+14.69x10^5s at 913°C (G.R.7x10^{-6}m/s;R=0.1, R.T.)	11	12.7	38	
"	DS+4.32x10^5s at 1121°C	9	11.5	38	"
	DS+25.9x10^5s at 1121°C (G.R.7x10^{-6}m/s;R=0.1, R.T.)	12	28.5	77	
	DS+4.32x10^5s at 1121°C (G.R.=47.6x10^{-6}m/s; R=0.1, R.T.)	25	27	44	

(Continued)

* ΔK_{TH} = minimum (threshold) stress intensity range for crack propagation.

** ΔK_C = critical stress intensity range for crack instability.

† DS = directionally solidified

†† R = stress ratio

††† G.R.= growth rate

†††† R.T.= room temperature

Table I. Continued

Composite	Condition	m	ΔK^{*}_{TH} ($MNm^{-3/2}$)	ΔK^{**}_{C} ($MNm^{-3/2}$)	Reference
Co,Cr-$(Cr,Co)_7C_3$	DS+240cycles(79-913°C)	18	23.7	45	This study
	DS+465cycles(79-913°C) ($G.R.7x10^{-6}$m/s; R=0.1, R.T.)	18	21.5	40.1	
"	DS+622cycles(79-1121°C)	11	11.6	35.2	"
	DS+704cycles(79-1121°C) ($G.R.7x10^{-6}$m/s; R=0.1 R.T.)	8	12.7	52.8	
"	DS, 760°C	5.7	-	-	8
	DS, 927°C	2.3	-	-	8
"	DS, R.T.	5 at $\Delta K=30$	9	47	10
	DS, 750°C	7 at $\Delta K=20$	9	29	10
	DS, 950°C	2.2 at $\Delta K=30$	9	55	10
CoTaC	DS, R.T.	4.6	7	64	9
$\gamma/\gamma'-\delta$	DS, R.T.	5.9	-	-	8
$\gamma-\delta$	DS, R.T.	4.9	-	-	7

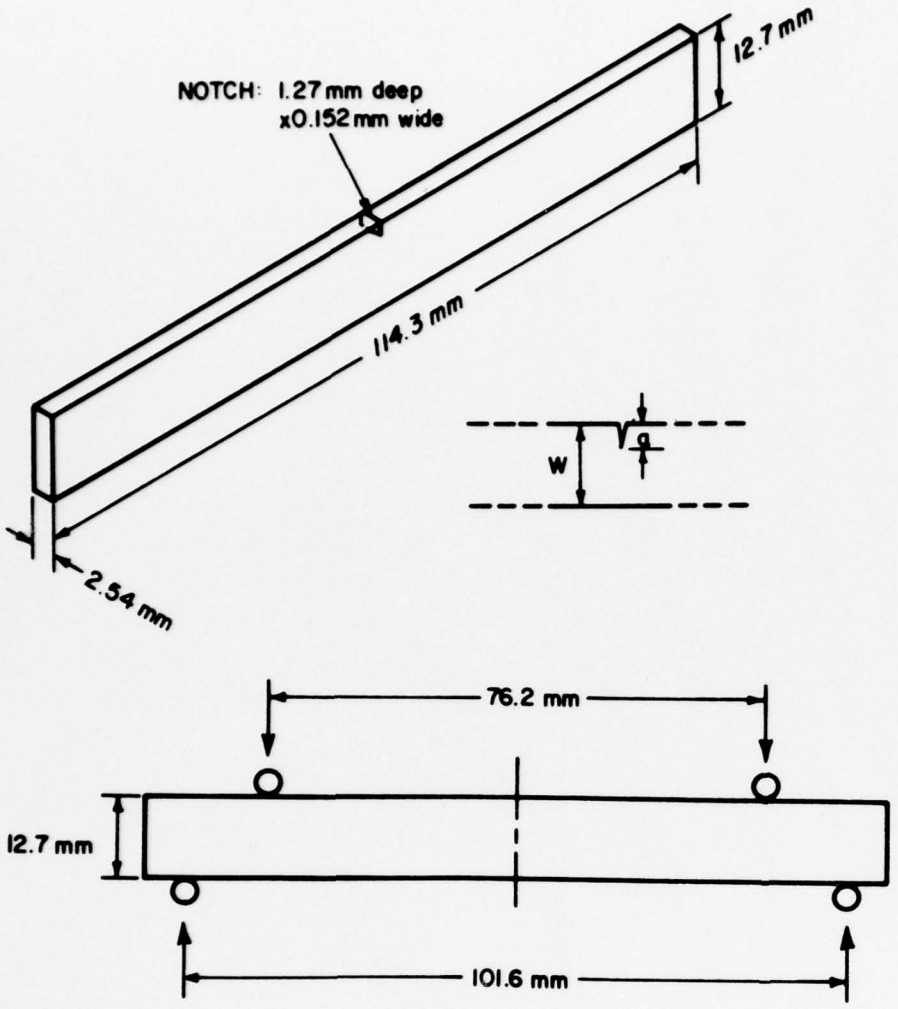

(a)

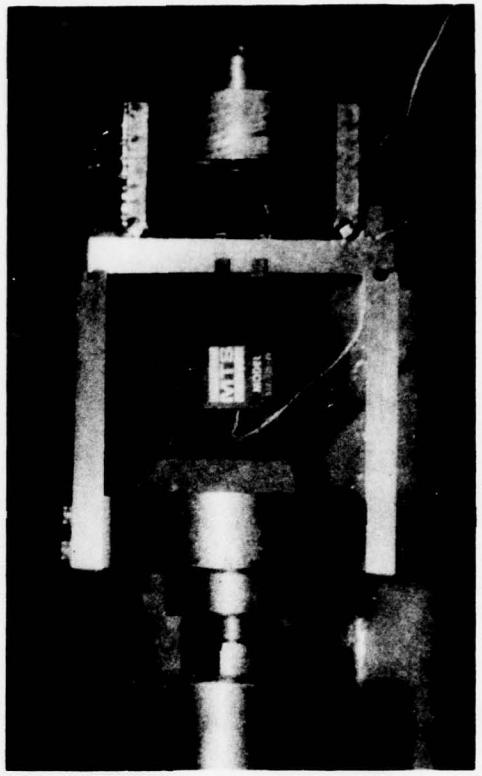

(b)

Figure 1: (a) Four-point bend specimen; (b) the bend fatigue facility with specimen and crack opening displacement gage in place.

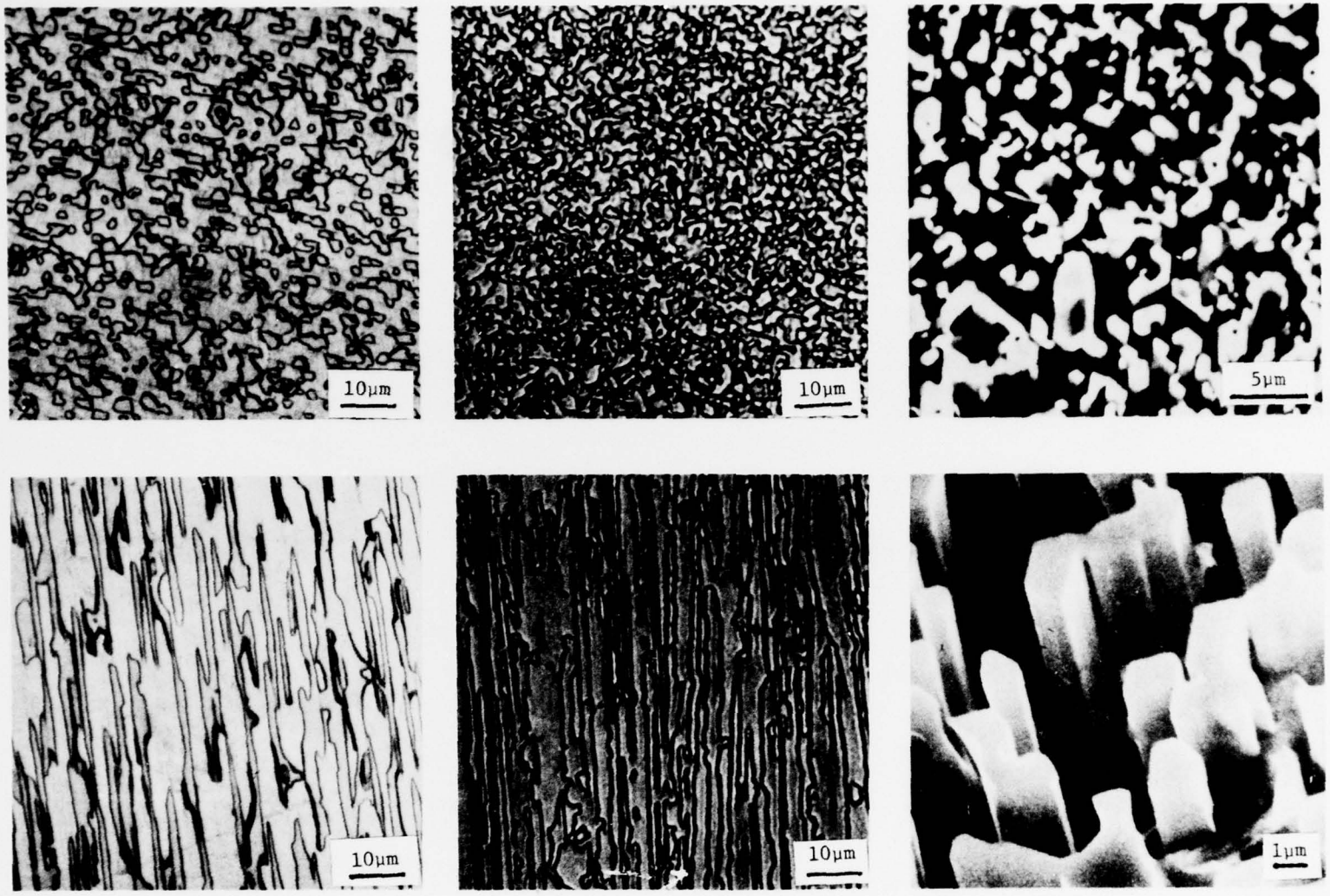

Figure 2: Transverse (a,c) and longitudinal (b,d) section optical micrographs and SEM (e,f). As-grown condition. Growth rate 7 x 10^{-6} m/s in a, b, e, and f; 47.6 x 10^{-6} m/s in c and d.

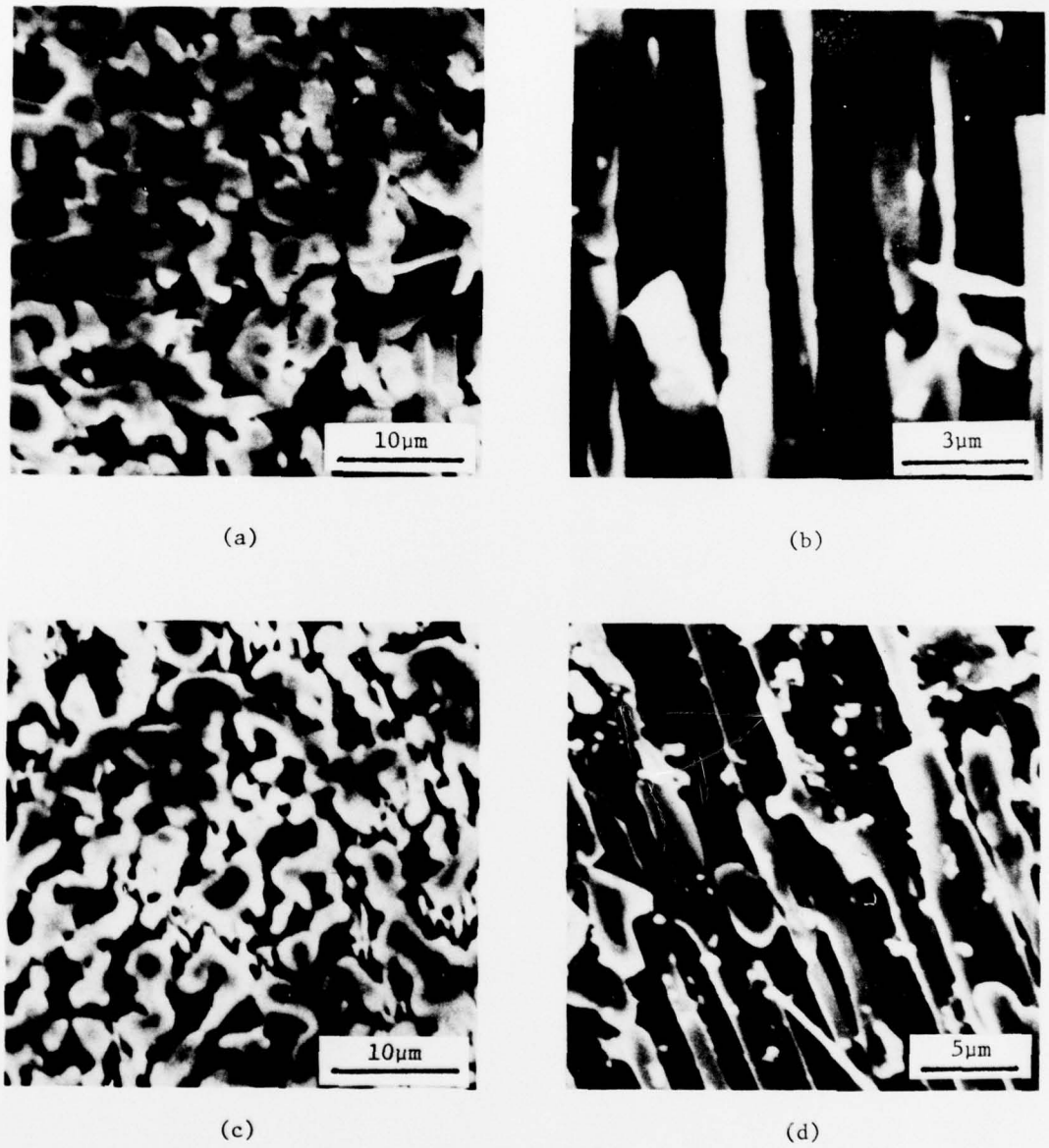

Figure 3: *SEM after exposure at 913°C; growth rate 7 x 10^{-6} m/s.*
(a) 25.92 x 10^4s; (b) 69.12 x 10^4s; (c) 10.37 x 10^5s;
(d) 19 x 10^5s.

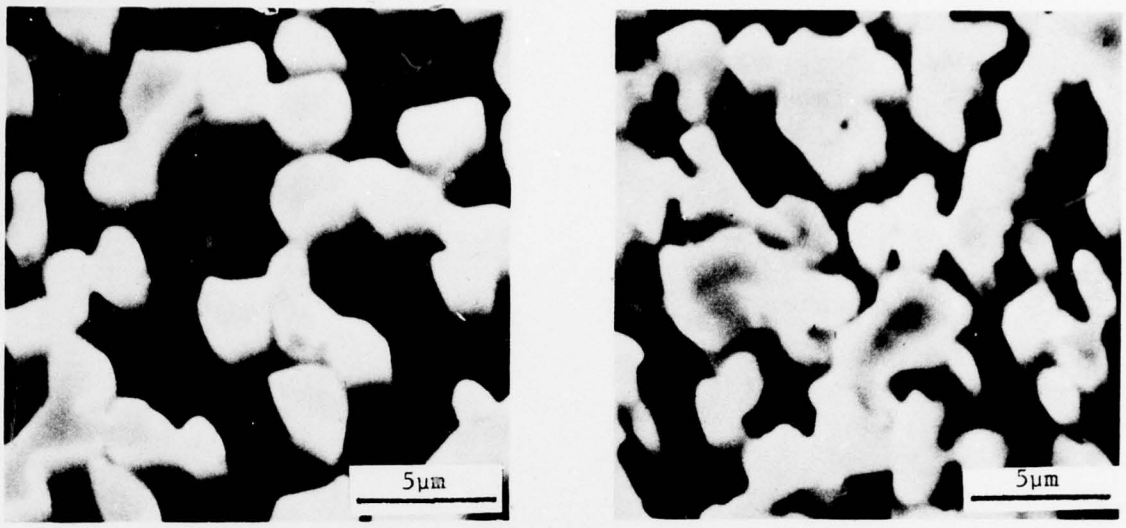

(a) (b)

Figure 4: SEM after exposure at 1121°C. (a) 34.56 x 10^4s, growth rate 7 x 10^{-6} m/s; (b) 25.92 x 10^5s, growth rate 47.6 x 10^{-6} m/s.

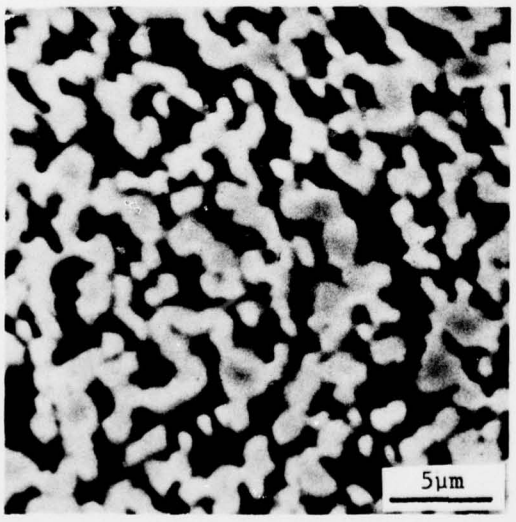

Figure 5: SEM after 466 cycles between 79°C and 913°C; growth rate 7 x 10^{-6} m/s.

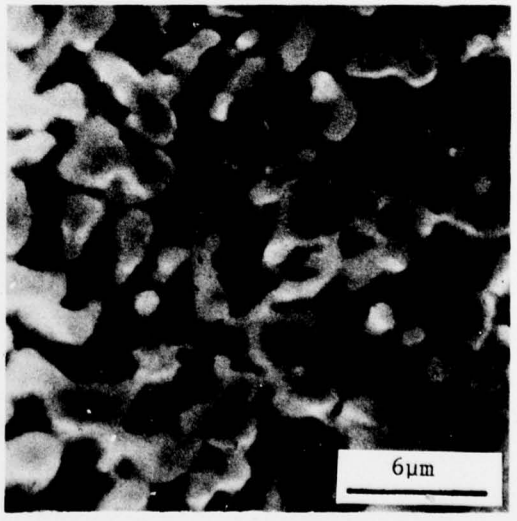

Figure 6: SEM after 693 cycles between 79°C and 1121°C; growth rate 7 x 10^{-6} m/s.

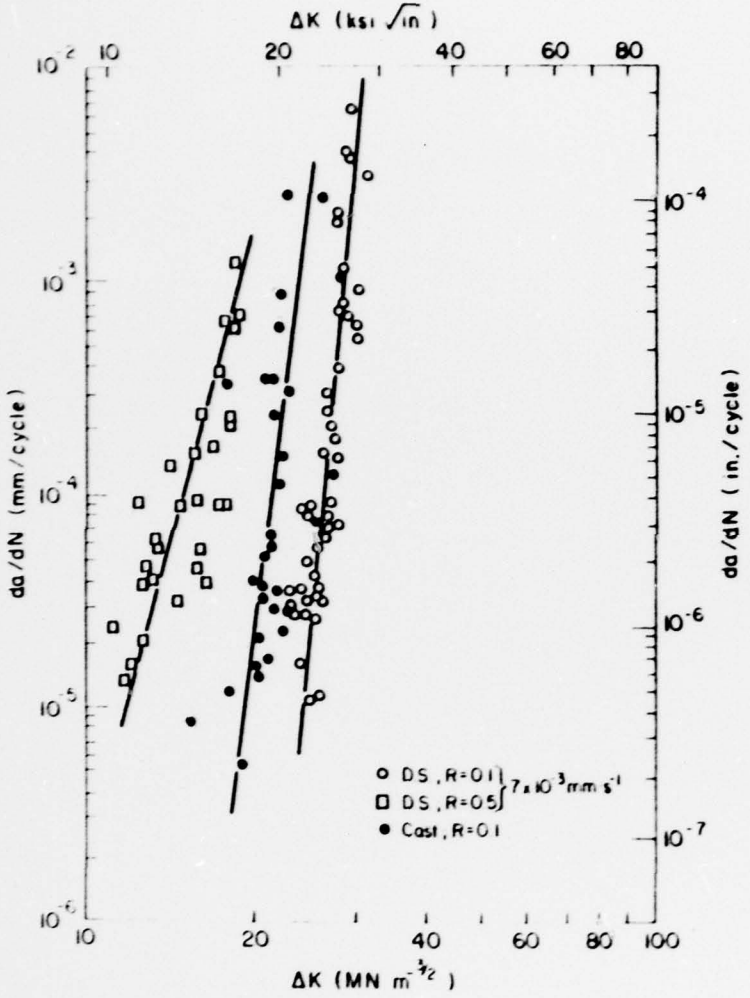

Figure 7: Crack propagation rate versus ΔK in the cast and directionally solidified (DS) conditions. Growth rate 7 x 10^{-6} m/s.

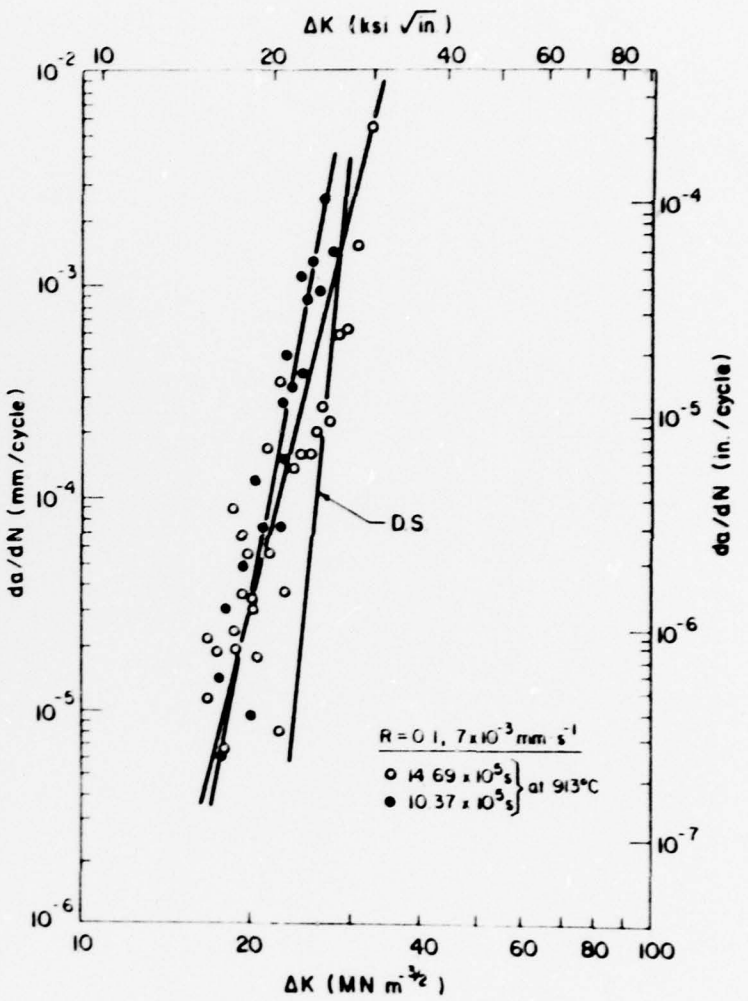

Figure 8: Crack propagation rate versus ΔK after exposure at 913°C. Growth rate 7 x 10^{-6} m/s.

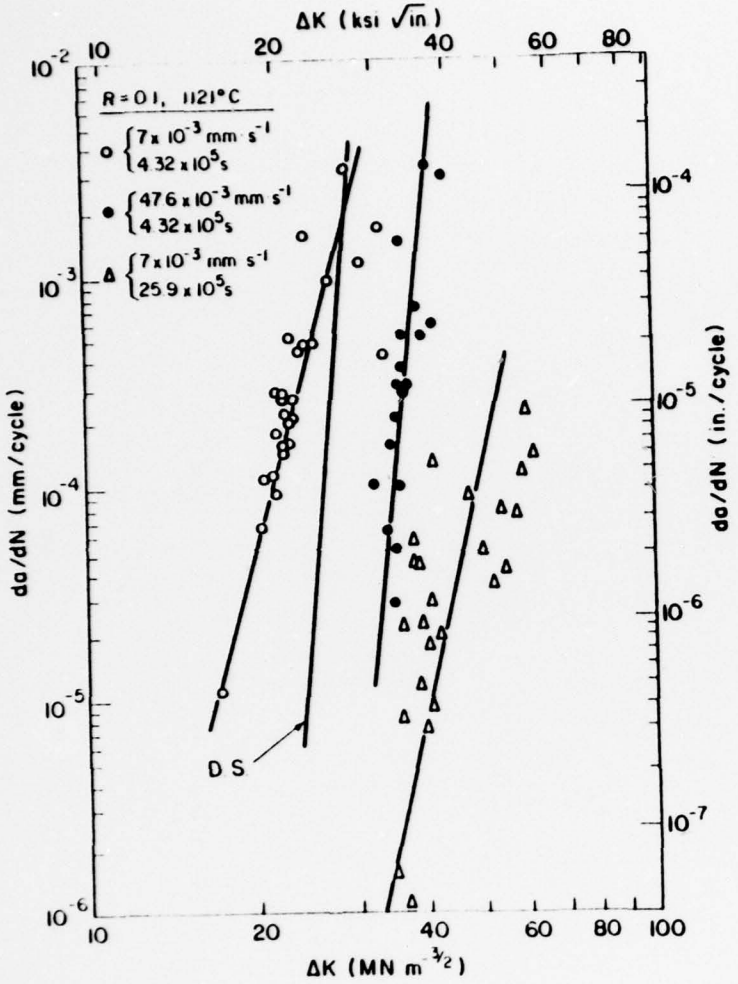

Figure 9: Crack propagation rate versus ΔK after exposure at 1121°C.

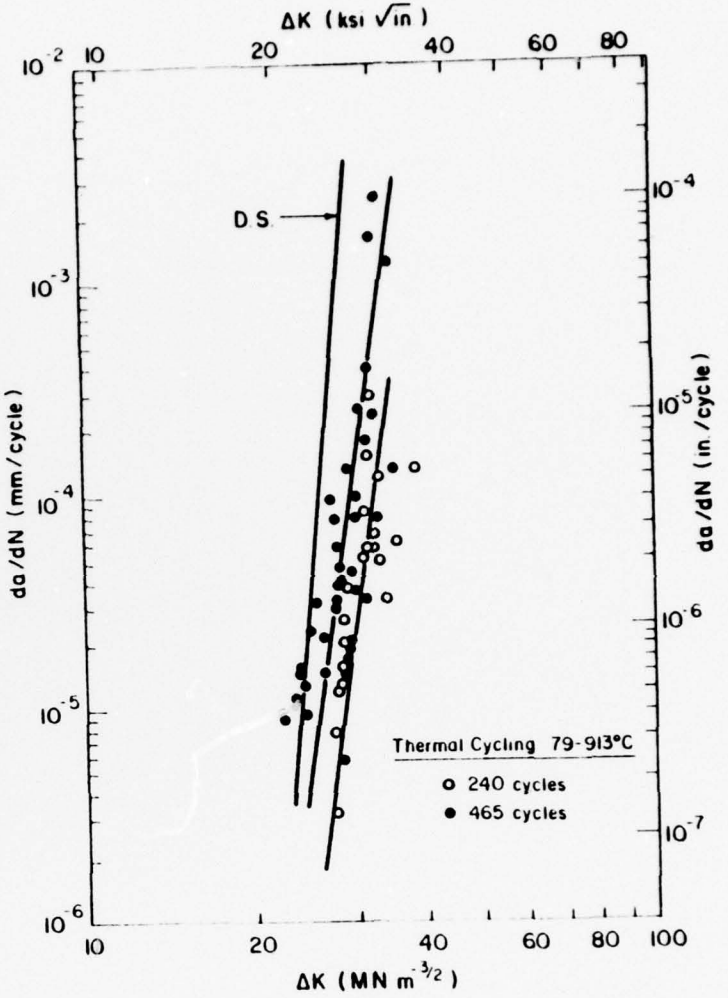

Figure 10: Crack propagation rate versus ΔK after thermal cycling between 79°C and 913°C. Growth rate 7 x 10^{-6} m/s.

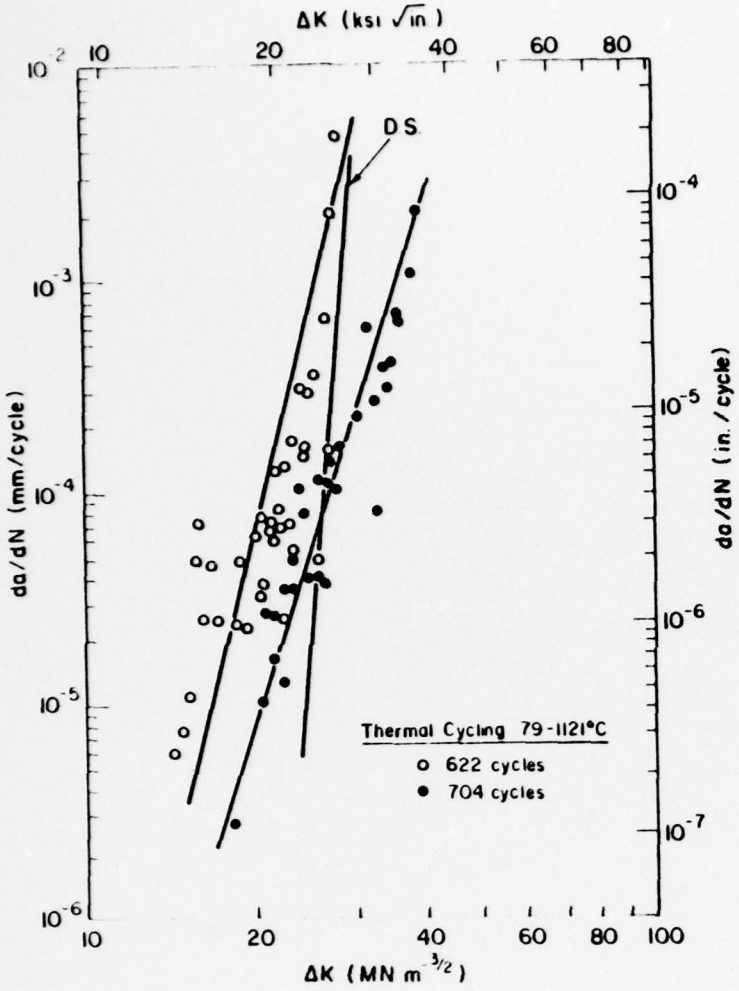

Figure 11: Crack propagation rate versus ΔK after thermal cycling between 79°C and 1121°C. Growth rate 7 x 10^{-6} m/s.

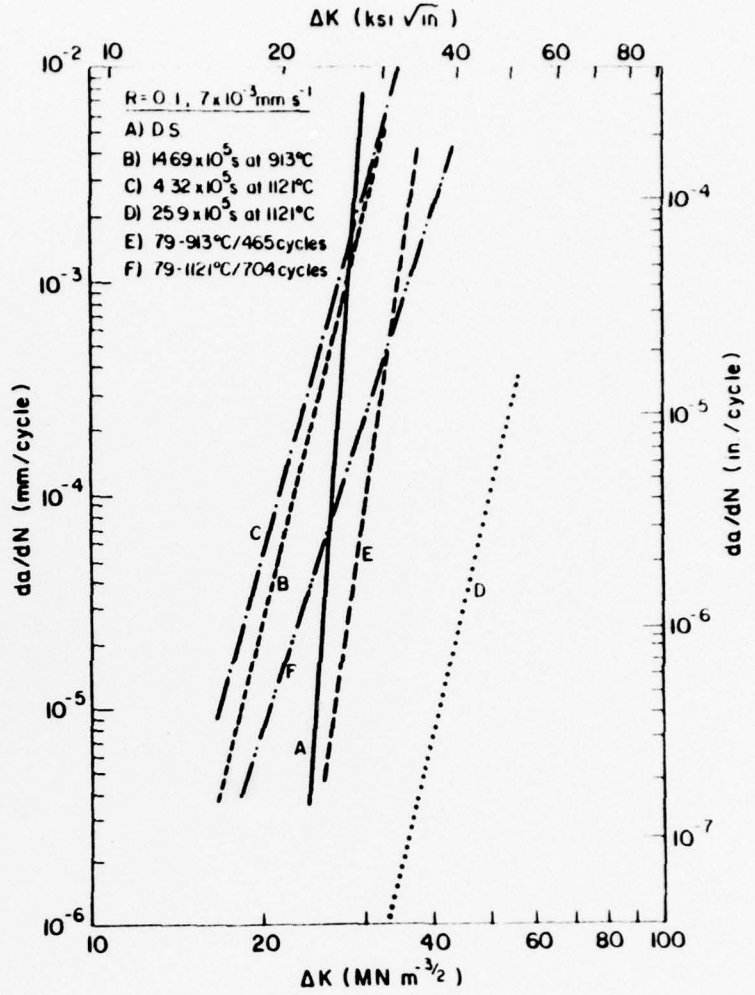

Figure 12: Crack propagation response as a function of thermal treatment.

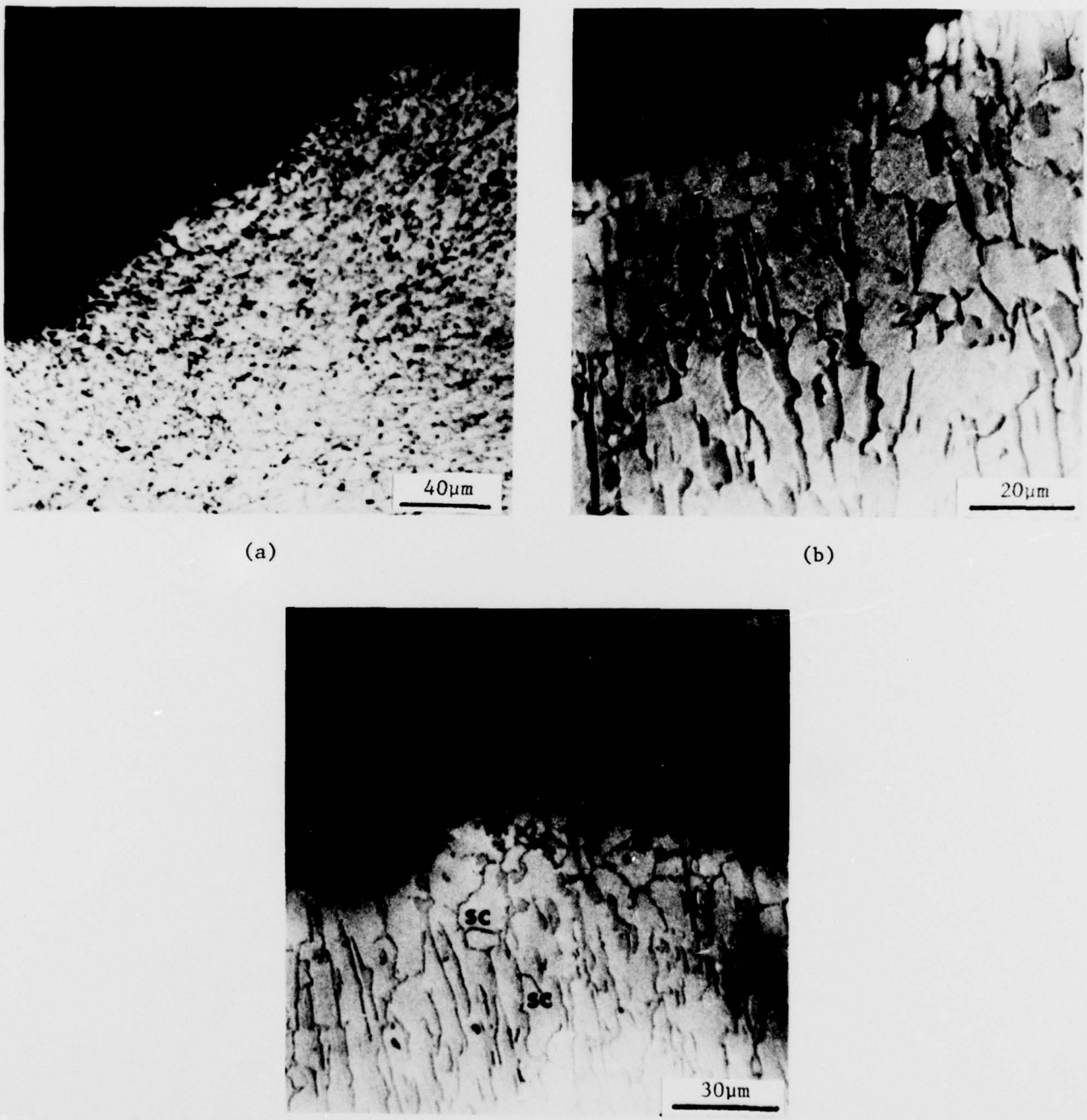

(a)

(b)

(c)

Figure 13: Optical micrographs of fracture surface profiles (a) Non-aligned (cast); (b) and (c) Directionally solidified, growth rate 7 x 10^{-6}m/s. SC = secondary matrix cracks.

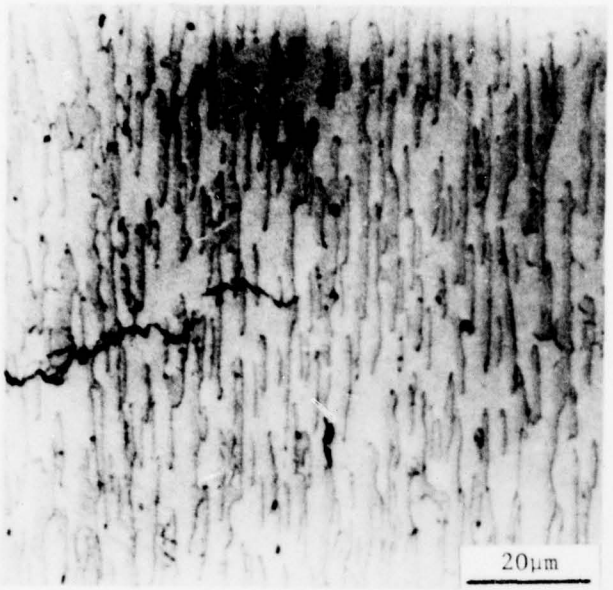

(a)

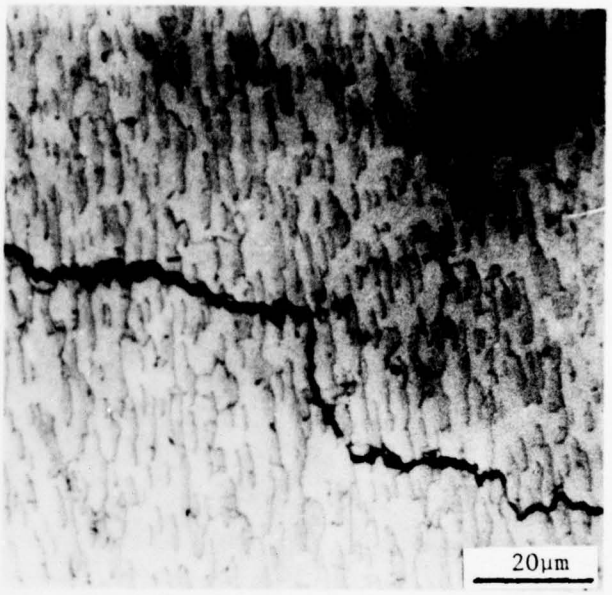

(b)

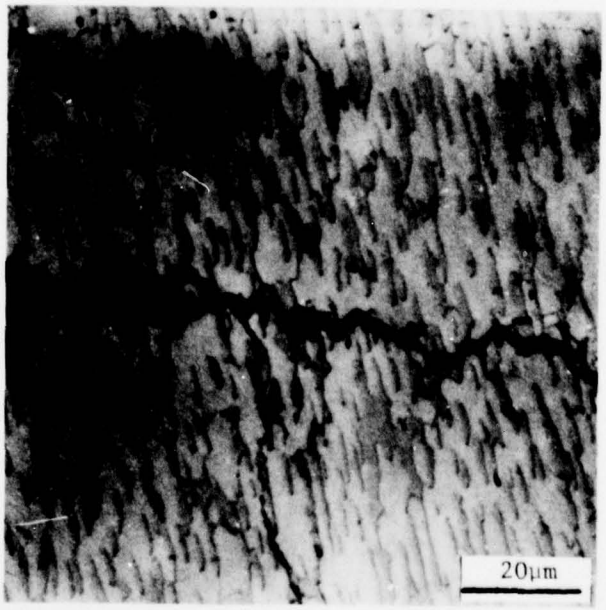

(c)

Figure 14: Optical micrographs of the crack form and path. (a) Vicinity of the crack tip, low ΔK (22 $MNm^{-3/2}$); (b) crack path at low ΔK (22 $MNm^{-3/2}$); (c) crack path at high ΔK (31 $MNm^{-3/2}$). Directionally solidified, growth rate 7×10^{-6} m/s.

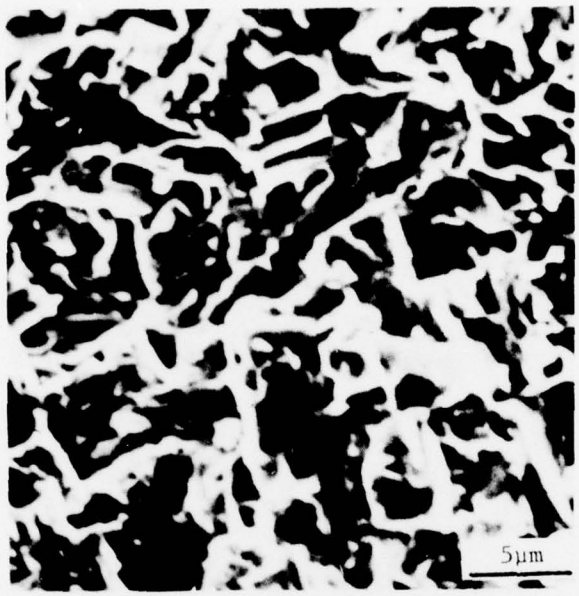

(a)

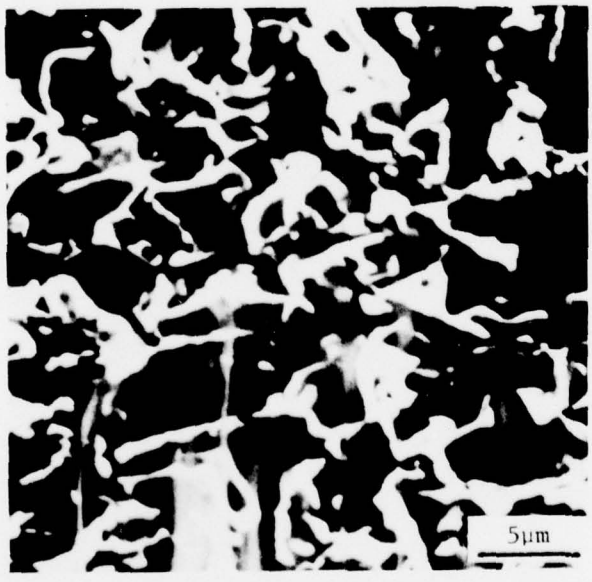

(b)

Figure 15. Fractographs (SEM) at (a) low ΔK (22 $MNm^{-3/2}$) and (b) high ΔK (31 $MNm^{-3/2}$). Directionally solidified, growth rate 7×10^{-6} m/s.

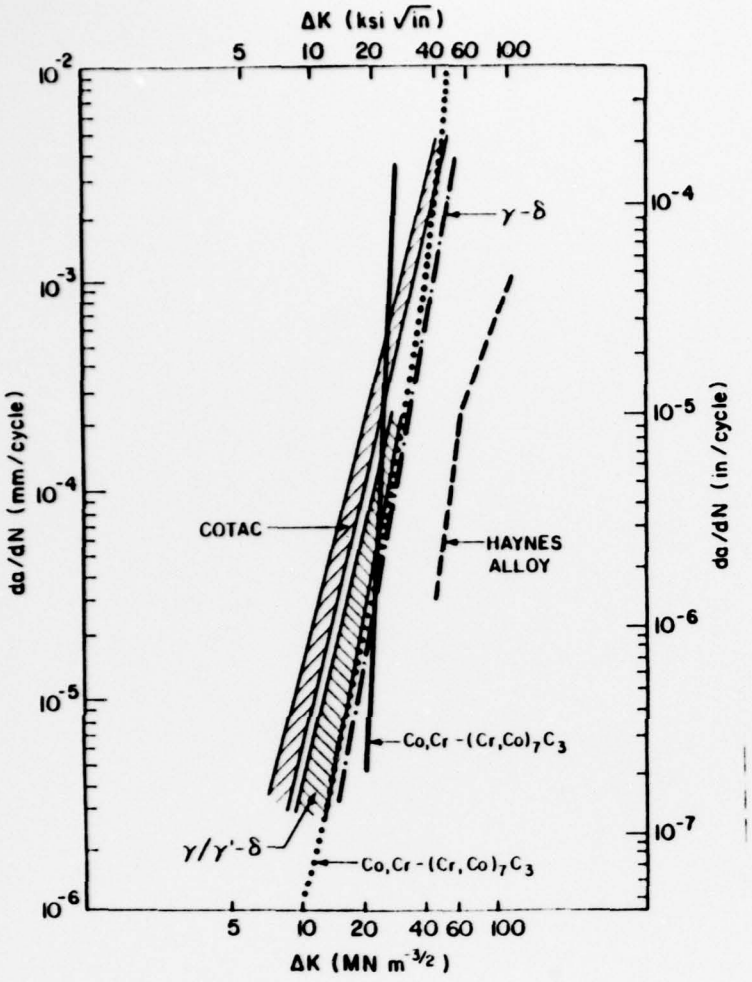

Figure 16. FCP of in-situ composites at room temperature. Cotac, γ-δ and γ/γ'-δ references (9), (7) and (8), respectively. ———— this study; · · · · · · reference (10).

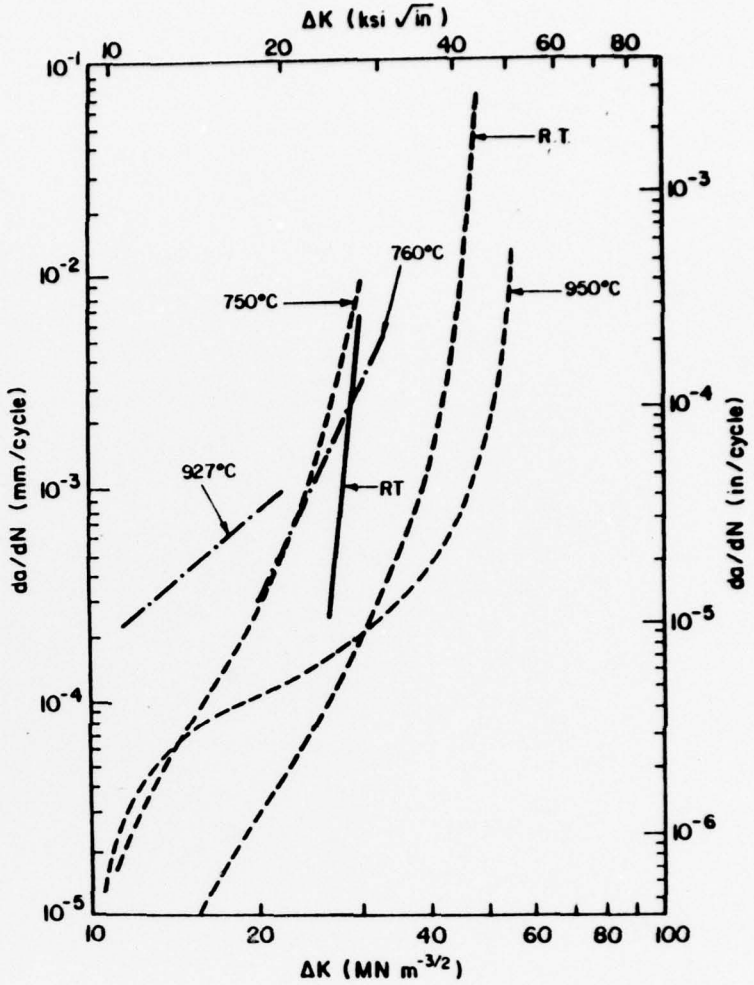

Figure 17: Effect of temperature on FCP of $Co,Cr-(Cr,Co)_7C_3$. — · — · — reference (8); — — — — — reference (10); ———— this study.

Appendix I. Calculation of ΔK and da/dN

- In pure (four-point) bending:

$$K = \frac{6YMa^{1/2}}{BW^2} \qquad \text{(A-1)}$$

where B is specimen thickness, W = specimen width, a = crack length, M is bending moment and Y is a function of(a/W) given in reference (29).

ΔK is the difference between K_{max} and K_{min} and $K_{min}/K_{max} = R$, the stress ratio.

- The crack length during the application of N cycles at a load range ΔP was taken as $(a_{initial} + a_{final})/2$. Values of 'a' were obtained from the output of the crack opening displacement gage converted to compliance versus crack length.

Unclassified

SECURITY CLASSIFICATION OF THIS PAGE (When Data Entered)

REPORT DOCUMENTATION PAGE		READ INSTRUCTIONS BEFORE COMPLETING FORM
1. REPORT NUMBER	2. GOVT ACCESSION NO.	3. RECIPIENT'S CATALOG NUMBER
4. TITLE (and Subtitle) Fatigue Crack Propagation in a $(Co,Cr)-(Cr,Co)_7C_3$ Composite		5. TYPE OF REPORT & PERIOD COVERED Technical Report December 1978 6. PERFORMING ORG. REPORT NUMBER
7. AUTHOR(s) M. H. Abdel Latif and A. Lawley		8. CONTRACT OR GRANT NUMBER(s) N00014-76-C-0205
9. PERFORMING ORGANIZATION NAME AND ADDRESS Department of Materials Engineering Drexel University Philadelphia, Pa. 19104		10. PROGRAM ELEMENT, PROJECT, TASK AREA & WORK UNIT NUMBERS
11. CONTROLLING OFFICE NAME AND ADDRESS Office of Naval Research Arlington, Va. 22217		12. REPORT DATE December 1978 13. NUMBER OF PAGES 32
14. MONITORING AGENCY NAME & ADDRESS(if different from Controlling Office)		15. SECURITY CLASS. (of this report) unclassified 15a. DECLASSIFICATION/DOWNGRADING SCHEDULE
16. DISTRIBUTION STATEMENT (of this Report) Unlimited DISTRIBUTION STATEMENT A Approved for public release; Distribution Unlimited		
17. DISTRIBUTION STATEMENT (of the abstract entered in Block 20, if different from Report)		
18. SUPPLEMENTARY NOTES		
19. KEY WORDS (Continue on reverse side if necessary and identify by block number) In-situ composite, cobalt-rich matrix, carbide reinforcement, isothermal exposure, thermal cycling, fatigue, crack propagation, fracture mechanics, fractography, microstructural change.		

20. ABSTRACT (Continue on reverse side if necessary and identify by block number)

Fatigue crack propagation in the $Co,Cr-(Cr,Co)_7C_3$ in-situ composite has been characterized at room temperature in the as-grown condition and following post-solidification isothermal exposure or thermal cycling. The dependence of da/dN on ΔK follows the Paris-Erdogan relation over the range $\Delta K \sim 10$ MN.m$^{-3/2}$ to ~ 50 MN.m$^{-3/2}$. Fracture toughness is low in the as-grown condition and is attributed to restricted matrix slip and a low stacking fault energy in the cobalt-rich matrix coupled with the absence of delamination. The heat treatments

DD FORM 1 JAN 73 1473 EDITION OF 1 NOV 65 IS OBSOLETE
S/N 0102-014-6601

Unclassified

SECURITY CLASSIFICATION OF THIS PAGE (When Data Entered)

delta K appox 10 MN/m (superscript 3/2) to 50 MN/m (superscript 3/2).

20. Continued

enhance fracture toughness and this is shown to be the result of precipitation of $(Co,Cr)_{23}C_6$ in the matrix and/or fiber coarsening with an attendant increase in the interfiber spacing. At the lower end of the ΔK range fatigue cracking is primarily crystallographic (stage I) in nature. Stage II cracking, with the fracture surface normal to the stress axis, is operative at the upper end of the ΔK range, the transition occurs between 17 $MN.m^{-3/2}$ and 28 $MN.m^{-3/2}$. The fracture toughness of $Co,Cr-(Cr,Co)_7C_3$ is inferior to CoTaC or the lamellar $\gamma/\gamma'-\delta$ and $\gamma-\delta$ in-situ composites. These differences are rationalized in terms of constituent matrix and fiber properties.